

Energy-transfer processes in Yb:Tm-doped KY₃F₁₀, LiYF₄, and BaY₂F₈ single crystals for laser operation at 1.5 and 2.3 μm

A. Braud, S. Girard, J. L. Doualan, M. Thuau, and R. Moncorgé

CIRIL, Laboratoire mixte CEA/CNRS/ISMRA, 6 Bd Maréchal Juin, 14050 CAEN Cedex, France

A. M. Tkachuk

S. I. Vavilov State Optical Institute, St. Petersburg 199034, Russia

(Received 7 June 1999; revised manuscript received 13 September 1999)

Energy-transfer processes have been quantitatively studied in various Tm:Yb-doped fluoride crystals. A comparison between the three host crystals which have been examined (KY₃F₁₀, LiYF₄, and BaY₂F₈) shows clearly that the efficiency of the Yb→Tm energy transfers is larger in KY₃F₁₀ than in LiYF₄ or BaY₂F₈. The dependence of the energy-transfer parameters upon the codopant concentrations has been experimentally measured and compared with the results calculated on the basis of migration-assisted energy-transfer models. Using these energy-transfer parameters and a rate equation model, we have performed a theoretical calculation of the laser thresholds for the ³H₄→³F₄ and ³H₄→³H₅ laser transitions of the Tm ion around 1.5 and 2.3 μm, respectively. Laser experiments performed at 1.5 μm in Yb:Tm:LiYF₄ then led to laser threshold values in good agreement with those derived theoretically. Based on these results, optimized values for the Yb and Tm dopant concentrations for typical values of laser cavity and pump modes were finally derived to minimize the threshold pump powers for the laser transitions around 1.5 and 2.3 μm.

I. INTRODUCTION

Since the pioneer work of F. Auzel,¹ it has been clearly recognized that a clever combination of sensitizer and activator ions could greatly enhance the efficiency of a rare-earth-doped laser material. Among all the sensitizers of interest, the Yb plays a singular role. It has the advantage to present only two multiplets (the ground-state level ²F_{7/2} and the excited-state level ²F_{5/2}) separated by ΔE ~ 10 000 cm⁻¹. This energy level diagram is highly favorable for efficient absorption of the high-power InGaAs laser diodes emitting around 950 nm and, at the same time, to avoid any undesirable excited-state absorption under intense optical pumping.

First investigations of Yb-sensitized materials were performed in the context of materials for infrared quantum counters (IRQC).^{2,3} Recent applications of conversion of IR into visible light are visualization of IR laser beams,⁴ three-dimensional display devices,⁵ or upconversion laser systems.⁶⁻⁸

Pr³⁺, Ho³⁺, Er³⁺, and Tm³⁺ ions were successively excited via energy-transfer processes starting from Yb³⁺ ions as sensitizers. Recently, laser operation of Tm:Yb:LiYF₄ at 1.5 and 2.3 μm originating from the ³H₄ to the ³F₄ and ³H₅ energy levels of the Tm³⁺ ion, respectively, were reported.^{9,10} The population mechanism for the ³H₄ emitting level includes two consecutive Yb→Tm energy transfers: ³H₆(Tm), ²F_{5/2}(Yb)→³H₅(Tm), ²F_{7/2}(Yb) and ³F₄(Tm), ²F_{5/2}(Yb)→³F₂, ³F₃(Tm), ²F_{7/2}(Yb). However, such population mechanism is relatively complex because the optical pumping cycle is also strongly affected by the Tm→Yb back transfers: ³H₄(Tm)+²F_{7/2}(Yb)→³H₆(Tm)+²F_{5/2}(Yb). Moreover, the second energy transfer, by reducing the effective lifetime of the lower excited-state level

³F₄, is essential to avoid any bottlenecking effect which would prevent the 1.5-μm laser emission under continuous-wave excitation. The sensitization of Tm³⁺ by Yb³⁺ was studied in the case of “true” upconversion effect where the emission wavelength was shorter than the excitation wavelength.^{11,12} Both ¹G₄ and ¹D₂ levels were populated after an excitation around 960 nm and led to efficient blue emissions respectively around 480 and 450 nm. The last step in the excitation process was carefully examined to separate forward and backward energy transfers between Tm and Yb necessary to reach such high energy levels. On the other hand, less attention was paid on the initial steps necessary to reach the ³F₄ and ³H₄ levels.

We present here a series of experiments made to analyze qualitatively and quantitatively the energy-transfer mechanisms resulting in the emissions starting from the ³H₄ down to the two lower excited states ³H₅ and ³F₄ levels of the Tm³⁺ ions. The data were obtained for three fluoride crystalline hosts KY₃F₁₀, LiYF₄, and BaY₂F₈ codoped with Tm and Yb. Fluoride materials have the advantage over oxides of reduced nonradiative deexcitation rates via multiphonon emissions ensuring relatively good fluorescence quantum efficiencies from the ³H₄ level. Compared to other low phonon energy materials such as chlorides, bromides, or sulfides, the fluorides present a reasonably high thermal conductivity, a good enough mechanical hardness, and a high chemical stability—in particular, a nonhygroscopic behavior. The three selected crystals were also chosen because they are single-site host materials for rare-earth (RE) ions which ensure homogeneously broadened absorption and emission spectra. This last point is especially crucial to investigate the multipolar interactions between ions as will be developed later. To obtain reliable measurements of the different parameters, we have performed short pulse excitations directly

TABLE I. Crystallographic properties of KY_3F_{10} , $LiYF_4$, and BaY_2F_8 .

	KY_3F_{10}	$LiYF_4$	BaY_2F_8
Structure	cubic (fluorite)	tetragonal (scheelite)	monoclinic ($BaTm_2F_8$ type)
Space group (Schoenflies)	$Fm\bar{3}m$ (O_h^5)	$I4_{1/a}$ (C_{4h}^6)	$C2/m$ (C_{2h}^3)
Crystallographic positions for Y^{3+} ions (coordination number)	$C_{4v}(8)$	$S_4(8)$	$C_2(8)$
Cell parameters	$a = 11.536 \text{ \AA}$	$a = 5.16 \text{ \AA}$ $c = 10.85 \text{ \AA}$	$a = 6.972 \text{ \AA}$ $b = 10.50 \text{ \AA}$ $c = 4.26 \text{ \AA}$ $\beta = 99^\circ 45'$
Number of elements by cell	8	4	2
Anisotropy	isotropic	uniaxial	biaxial
Melting point	$\approx 990 \text{ }^\circ\text{C}$ (congruent)	$\approx 810 \text{ }^\circ\text{C}$ (incongruent)	$\approx 1000 \text{ }^\circ\text{C}$ (congruent)

into the 3F_4 and 3H_4 levels of the thulium ions and into the $^2F_{5/2}$ of the ytterbium ions. Using increasing excitation intensities, it was possible to discriminate between the different energy-transfer parameters involved in the Tm-Yb-codoped fluoride crystals.

The results were systematically compared, in the case of dominant energy migration, with those deduced from the fitting of the measured fluorescence data to the rate equation model. The experiments were then completed by recording the rise time obtained after square-pulse-shape excitation of the Yb ions. The efficiency of the ytterbium codoping as deactivator, to avoid the bottlenecking effect for the transition $^3H_4 \rightarrow ^3F_4$ and to recycle the energy back into the upper laser level for stimulated emissions around 1.5 and 2.3 μm , is also discussed and the properties of the different studied fluoride crystals are compared.

II. MATERIAL PREPARATION

Crystals of KY_3F_{10} , $LiYF_4$, and BaY_2F_8 singly doped with Tm^{3+} and codoped with Tm^{3+} and Yb^{3+} were grown by using the Czochralski method in a homemade pulling apparatus especially designed for fluoride materials. Great care was taken during the crystal growth to control the fluorinating atmosphere (mixture of Ar and CF_4) and to avoid melt contamination with oxygen or hydroxide as already described elsewhere.¹³

KY_3F_{10} is an isotropic crystal with a cubic-face-centered structure $Fm\bar{3}m$ (O_h^5) similar to the fluorite structure.¹⁴ The elementary cell contains eight formula units and has a cell parameter $a = 11.54 \text{ \AA}$. The trivalent rare-earth dopants substitute for the yttrium ions in sites of C_{4v} symmetry. KY_3F_{10} is relatively easy to grow compared to other fluoride materials, melting congruently at $T = 990 \text{ }^\circ\text{C}$ as confirmed recently by reinvestigation of the phase diagram of the KF-YF₃ system.¹⁵

$LiYF_4$ is a uniaxial fluoride crystal well known as an efficient active medium for solid-state lasers with different rare-earth ions. It has a tetragonal structure similar to

$CaWO_4$ -scheelite structure with space group $I4_{1/a}$ (C_{4h}^6) and a point symmetry group S_4 corresponding to the site of the Y^{3+} ions. Czochralski pulling method is especially well-adapted to grow $LiYF_4$ because of the incongruently melting behavior of this material with a peritectic composition of 49:51 (YF₃ to LiF ratio) at $842 \text{ }^\circ\text{C}$, as recently redetermined.¹⁶

BaY_2F_8 is a biaxial crystal with monoclinic structure—space group $C2/m$ (C_{2h}^3)—with a crystallographic position for the RE of C_2 symmetry. It is isomorphic to $BaTm_2F_8$ and has a congruent melting point at $T = 960 \text{ }^\circ\text{C}$.¹⁷ Recent studies have demonstrated the interest of BaY_2F_8 codoped with Tm and Yb for upconversion laser systems.¹⁸ Compared to $LiYF_4$, it has a lower maximum phonon energy which significantly reduces the nonradiative decay rates. Physical properties of KY_3F_{10} , $LiYF_4$, and BaY_2F_8 are summarized in Table I.

After crystal growth and annealing, samples were oriented by x-ray-back-reflexion Laue techniques. For BaY_2F_8 , the sample was initially cut with two sides normal to the (010) direction. This twofold-symmetry axis of the crystal corresponds to one of the principal axes of the optical indicatrix, labeled axis 2. The sample was then placed between crossed polarizers and the two other dielectric axes were identified as the extinction directions when the sample was turned around (010). The three principal axes were labeled following the notation used by R. A. McFarlane.¹⁹ The principal axis oriented 21° from the c axis was identified as axis 3 whereas the orthogonal axis in the plane normal to axis 2 was labeled axis 1. Compared to the notation used by L. D. DeLoach²⁰ for the measurements of the absorption and emission spectra of Yb^{3+} in BaY_2F_8 , the axis 1 corresponds to z , the axis 2 to y , and the axis 3 to x .

The nominal Tm^{3+} concentrations were varied between 0.5% and 1% and the Yb^{3+} concentrations between 1% and 15%. Singly doped samples with a low concentration of Yb^{3+} (between 0.1 and 0.5%) were also grown to determine the fluorescence lifetime of the $^2F_{5/2}$ level in the absence of Tm-Yb energy transfers or radiation trapping effects. After

TABLE II. Concentration of Tm^{3+} and Yb^{3+} in the different samples of LiYF_4 , and KY_3F_{10} , and BaY_2F_8 . A concentration of 1 at. % represents 1.39×10^{20} ions/cm³ in LiYF_4 , 1.57×10^{20} ions/cm³ in KY_3F_{10} and 1.28×10^{20} ions/cm³ in BaY_2F_8 .

Sample	Number	Nominal concentration (before crystal growth)	After growth ion concentration (cm ⁻³)
LiYF_4	1	1% Tm	1.21×10^{20} Tm
LiYF_4	2	0.5% Tm:5% Yb	0.67×10^{20} Tm/ 6.8×10^{20} Yb
LiYF_4	3	0.5% Tm:7% Yb	0.71×10^{20} Tm/ 8.5×10^{20} Yb
LiYF_4	4	1% Tm:5% Yb	1.2×10^{20} Tm/ 7×10^{20} Yb
LiYF_4	5	1% Tm:10% Yb	1.38×10^{20} Tm/ 12.2×10^{20} Yb
LiYF_4	6	1% Tm:15% Yb	1.2×10^{20} Tm/ 18.9×10^{20} Yb
KY_3F_{10}	7	1% Tm	1.37×10^{20} Tm
KY_3F_{10}	8	0.5% Tm:5% Yb	0.74×10^{20} Tm/ 7.4×10^{20} Yb
KY_3F_{10}	9	1% Tm:5% Yb	1.3×10^{20} Tm/ 7×10^{20} Yb
BaY_2F_8	10	1% Tm	1.08×10^{20} Tm
BaY_2F_8	11	0.5% Tm:5% Yb	0.8×10^{20} Tm/ 6.94×10^{20} Yb

crystal growth, the final dopant concentration was determined by inductively coupled plasma (ICP) analysis. Table II contains the nominal and the real dopant concentrations of the samples.

III. OPTICAL MEASUREMENTS

The absorption spectra were recorded with a Perkin-Elmer Lambda 9 double beam spectrophotometer. A Glan-Thompson birefringent polarizer was added before the beam-splitter to record polarized spectra for the anisotropic host materials— LiYF_4 and BaY_2F_8 .

The emission spectra and the fluorescence decays were obtained by exciting the samples with a wide-band optical parametric oscillator (GWU OPO model C-355) pumped by the third harmonic of a *Q*-switched Nd:YAG laser (Spectron model 404G). All the emission spectra were taken by a single grating spectrometer (25-cm focal length ORIEL monochromator) equipped with a 600 grooves/mm grating blazed at $\lambda_B = 750$ nm or a 300 grooves/mm grating blazed at $\lambda_B = 2$ μm . The signal was detected by a photomultiplier tube with an extended response in the near infrared spectral region (Hamamatsu model R5108) or two InGaAs photodiodes cooled with Peltier element (Hamamatsu model G5832-23 and G5852-21). Then, it was fed into a Princeton Applied Research Model 162 boxcar integrator and processed by a personal computer interfaced with an analog/digital converter. The computer also controls the rotation of the spectrometer grating via a stepper motor. The spectral response of the system was recorded by means of a calibrated tungsten lamp.

The fluorescence decays were acquired at discrete wavelengths corresponding to clearly identified optical transitions of the Tm^{3+} and Yb^{3+} ions. The transient signals were averaged and stored with a fast digital oscilloscope (Tektronix TDS 350). To reduce the radiation trapping effects which affect the fluorescence signal, for example, in Yb:YAG ,²¹ the fluorescence lifetimes were recorded after excitation of thin powdered samples. The fluorescence kinetics during and after excitation with square-shape pulses were studied using a CW InGaAs laser diode emitting at 960 nm (SDL model

6362-P1), directly modulated using an external square pulse generator to drive the injected current into the emitting junction.

The excited-state absorption cross section corresponding to the ${}^3F_4 \rightarrow {}^3F_2$ transition was measured by using an experimental setup²² based on a pump-probe technique in which the probe beam is provided by a broadband tungsten-halogen lamp and the pump by a homemade continuously tunable (between 1.45 and 1.75 μm) color center laser (CCL) with $(F_2^+)_H$ in NaCl:OH as active centers.

IV. FIRST STEP ENERGY-TRANSFER RESULTS

The first energy-transfer mechanism involved in the 1.5- and 2.3- μm laser emissions of Tm:Yb-codoped fluorides is illustrated in Fig. 1. After excitation into their ${}^2F_{5/2}$ level, the Yb ions transfer their energy to the Tm ions via multipolar interactions. This first step—called step 1 in the following—can be summarized as

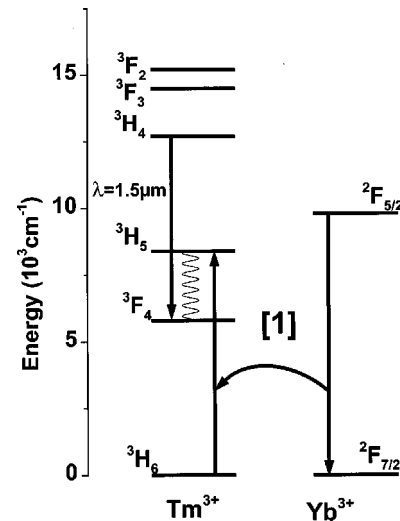


FIG. 1. Scheme for energy-transfer step 1 between Yb^{3+} and Tm^{3+} ions.

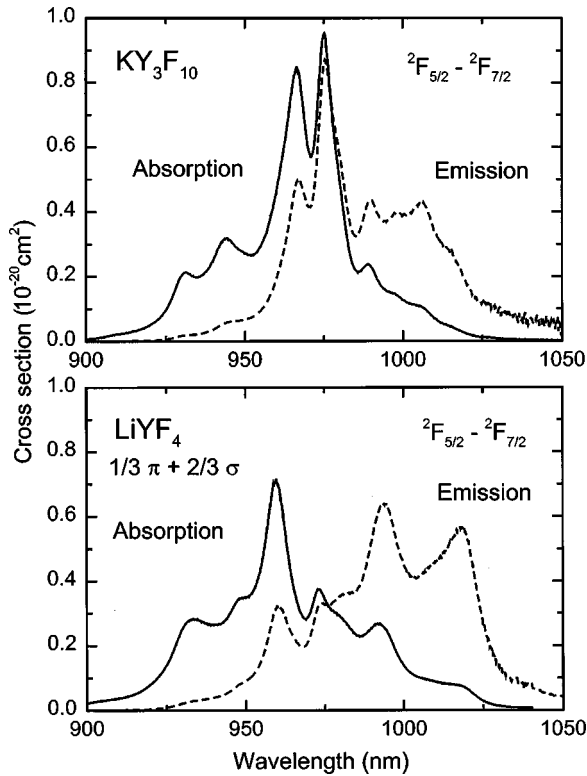
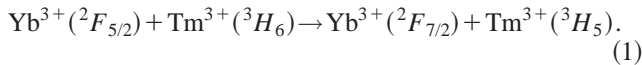


FIG. 2. ${}^2F_{7/2} \rightarrow {}^2F_{5/2}$ absorption and emission spectra of Yb^{3+} in LiYF_4 and in KY_3F_{10} .



It is immediately followed by a fast multiphonon relaxation from level 3H_5 down to the metastable level 3F_4 . Energy-transfer step 1 is far from being resonant—the energy mismatch, which is defined as the energy gap between the lowest sublevel of the ${}^2F_{5/2}$ level and the highest sublevel of the 3H_5 multiplet, is nearly equal to $\Delta E \sim 1300 \text{ cm}^{-1}$ and necessitates the emission of at least three phonons in fluoride crystals (the maximum phonon energy of which being $\hbar\omega = 500 \text{ cm}^{-1}$). Because the energy of the Yb ions before step 1 exceeds the final energy of the Tm ions, the energy transfer could be qualified as an exoenergetic energy transfer with a relatively high probability compared to an endoenergetic one. The other favorable factor to step 1 resides in the fact that the absorption and emission spectra of the Yb ions overlap very strongly (Fig. 2). This greatly enhances the energy migration among the Yb ions. As it is well known since the early works of Yokota and Tanimoto²³ and Burshtein,²⁴ the migration assisted energy transfers significantly increase the probability of interaction between sensitizer and activator ions of different species. The excitation energy jumps from one excited sensitizer site to a neighboring one until it reaches a sensitizer close enough to an activator to allow efficient energy transfer. Moreover, when the energy-transfer efficiency is reduced by back transfers from the activators to the sensitizers, the migration may favor the transfer sensitizer→activator compared to the back transfer because of the relative concentrations of the codopants ($N_S \gg N_A$).

The energy transfer between Yb and Tm represented by Eq. (1) can be clearly evidenced by comparing the fluores-

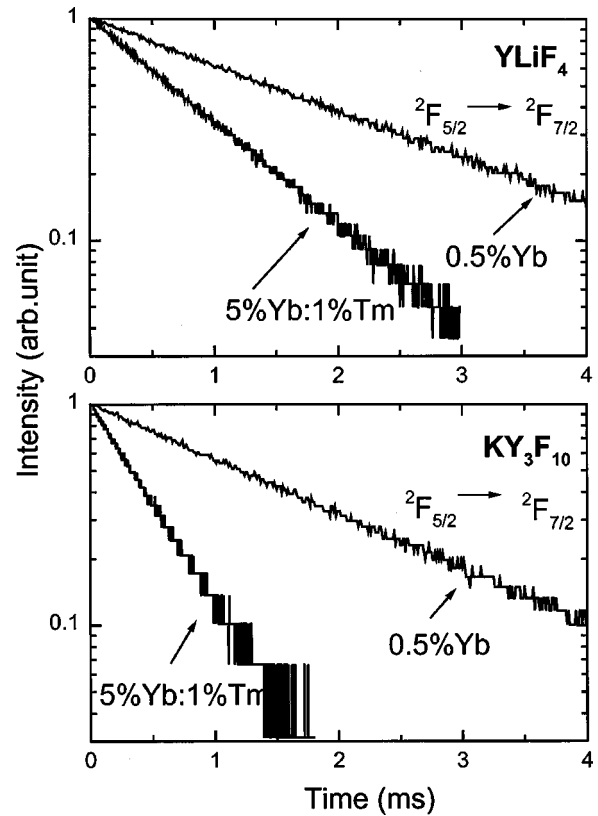


FIG. 3. Examples of decay curves from the ${}^2F_{5/2}$ level in singly doped LiYF_4 and KY_3F_{10} and codoped with Yb^{3+} and Tm^{3+} ions.

cence decays of the Yb^{3+} ions (transition ${}^2F_{5/2} \rightarrow {}^2F_{7/2}$) in a singly doped crystal and in Tm:Yb codoped crystals after direct excitation of the Yb with nanosecond laser pulses at $\lambda = 960 \text{ nm}$. The samples singly and codoped with Tm:Yb were carefully crushed and thin layers of powder were pressed between two glass slides. The layer thickness was reduced as much as possible to avoid radiation trapping effects while keeping a reasonably high fluorescence signal-to-noise ratio. To control that reabsorption had only limited effects on our experimental measurements, a comparison was made between the emission cross-section spectra obtained by using the reciprocity method and the Fuchtbauer-Ladenburg formula, assuming $\tau_R = \tau_F$.²⁵ When bulk samples or thick powdered layers were used, the emission spectra that were derived by using the two methods were significantly different, i.e., the relative peak intensity of the spectrum obtained from the emission line shape function was systematically smaller than that appearing on the emission spectrum deduced from the absorption. The distortion, attributed to the reabsorption from the ground-state level, disappears when the layer of the powdered sample was thin enough. The total internal reflexion that could appear within each individual grain of powder has less effect in a fluoride than in an oxide material such as YAG or YVO_4 because of the lower refractive index. Therefore no further attempt was made to use the method described by Sumida *et al.*²⁰ to avoid radiation trapping. Figure 3 shows the decay curves recorded for codoped LiYf_4 and KY_3F_{10} samples compared to the decay curves recorded for singly doped Yb: LiYF_4 and Yb: KY_3F_{10} crystals. Similar results were observed in the case of Yb:Tm: BaY_2F_8 . As shown in Fig. 3, the fluorescence decay

TABLE III. Lifetimes of the ${}^2F_{5/2}$ level in singly doped crystals and codoped with Yb^{3+} and Tm^{3+} and energy-transfer parameters W_1 ($10^{-18} \text{ cm}^{-3} \text{ s}^{-1}$) for energy-transfer step 1.

Sample	$\tau({}^2F_{5/2})_{\text{Yb}}$ (msec)	$\tau({}^2F_{5/2})_{\text{Yb,Tm}}$ (msec)	W_1
LiYF ₄ :0.5% Yb (no. 12)	2.1		
LiYF ₄ :0.5% Tm:5% Yb (no. 2)	2.1	1.26	4.7
LiYF ₄ :0.5% Tm:7% Yb (no. 3)	2.1	1.09	6.2
LiYF ₄ :1% Tm:5% Yb (no. 4)	2.1	0.85	5.8
LiYF ₄ :1% Tm:10% Yb (no. 5)	2.1	0.57	9.1
LiYF ₄ :1% Tm:15% Yb (no. 6)	2.1	0.6	9.9
KY ₃ F ₁₀ :0.5% Yb (no. 13)	1.77		
KY ₃ F ₁₀ :0.5% Tm:5% Yb (no. 8)	1.77	0.66	12.8
KY ₃ F ₁₀ :1% Tm:5% Yb (no. 9)	1.77	0.44	13.1
BaY ₂ F ₈ :0.5% Tm:5% Yb (no. 11)	2.04 ^a	1.09	5.1

^aReference 12.

curves exhibit in all cases a single exponential behavior typically over three e -folding times. The excitation pulse intensity was limited to avoid any undesirable upconversion effect. The exponential decay mode of the Yb fluorescence in the codoped systems is characteristic of migration assisted energy transfer. In the simplest model, the energy-transfer rate can be directly determined by using the fluorescence lifetimes $\tau({}^2F_{5/2})_{\text{Yb}}$ and $\tau({}^2F_{5/2})_{\text{Yb,Tm}}$ measured in the singly doped and codoped samples, respectively. Indeed, the dynamics for the ${}^2F_{5/2}$ level population can be described by the rate equation

$$\frac{dn({}^2F_{5/2})_{\text{Yb}}}{dt} = -\frac{n({}^2F_{5/2})_{\text{Yb}}}{\tau({}^2F_{5/2})_{\text{Yb}}} - K_1 n({}^2F_{5/2})_{\text{Yb}}, \quad (2)$$

where K_1 represents the energy-transfer probability for step 1. We will also use the energy-transfer parameter W_1 which is related to the energy migration probability by $K_1 = n({}^3H_6)_{\text{Tm}} \times W_1$. Assuming that the migration-assisted energy transfers strongly dominate over the direct sensitizer-activator transfers, the energy-transfer probability is found time-independent and can be related to the effective lifetimes by

$$K_1 = \frac{1}{\tau({}^2F_{5/2})_{\text{Yb-Tm}}} - \frac{1}{\tau({}^2F_{5/2})_{\text{Yb}}}. \quad (3)$$

However, the sensitizer and the activator concentrations used in our study never reach the critical regime known as the fast migration regime where the energy-transfer parameter becomes a value independent of the sensitizer concentration. Therefore W_1 must be determined for each composition to be effectively usable in rate equations. The thulium ion density brought into the 3F_4 level is kept low enough to assume $n({}^3H_6)_{\text{Tm}}$ equal to the thulium concentration. The different values of W_1 deduced from Eq. (3) for each sample are listed in Table III. Considering crystals with similar Yb and Tm concentrations (samples 1, 6, and 8), W_1 turns out to be much larger in KY₃F₁₀ than in LiYF₄ or BaY₂F₈.

To describe more precisely the dependence of the energy-transfer probability K_1 with the concentrations of Tm and Yb

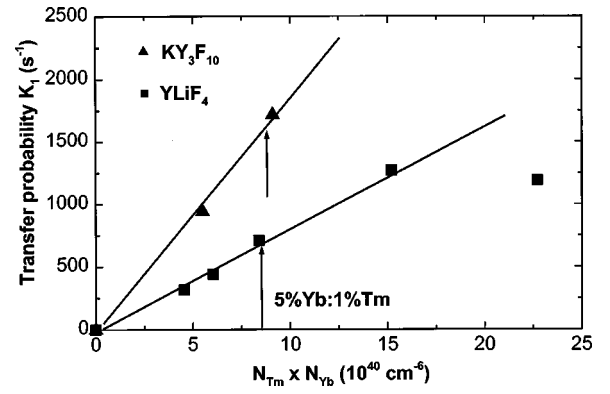


FIG. 4. Variation of the energy-transfer probability K_1 for the energy-transfer step 1 as a function of the product $N_{\text{Tm}} \times N_{\text{Yb}}$.

ions, we have plotted in Fig. 4 the value of K_1 versus the product $N_{\text{Tm}} \times N_{\text{Yb}}$ in the case of KY₃F₁₀ and LiYF₄. As can be seen in the case of LiYF₄, below a critical Yb concentration of about 15%, the energy-transfer probability for the first step can be expressed as

$$K_1 = N_{\text{Tm}} \times N_{\text{Yb}} \times \alpha_1 \quad (4)$$

and consequently

$$W_1 = N_{\text{Yb}} \times \alpha_1, \quad (5)$$

where α_1 is a constant equal to $\alpha_1 = 0.85 \times 10^{-38} \text{ cm}^6 \text{ s}^{-1}$ in LiYF₄ and $\alpha_1 = 1.87 \times 10^{-38} \text{ cm}^6 \text{ s}^{-1}$ in KY₃F₁₀, which again shows clearly that energy transfers are more efficient in KY₃F₁₀ than in LiYF₄. Relation (4) is consistent both with the migration-assisted energy-transfer models from Yokota and Tanimoto and Burshtein. In both models, the migration-controlled energy-transfer probability is linearly dependent on the product of the codopant concentrations. In the Burshtein model (also called the hopping model), which applies when the probability of energy migration among the Yb sensitizers is higher than the probability for direct Yb→Tm energy transfer on the microscopic scale—which should be the case here because of the nonresonance between the ${}^3H_5(\text{Tm})$ and ${}^2F_{5/2}(\text{Yb})$ levels— $K_1 = K_H$ with

$$K_H = [\pi(2\pi/3)^{5/2} C_{\text{YbTm}}^{1/2} C_{\text{YbYb}}^{1/2}] N_{\text{Tm}} N_{\text{Yb}}, \quad (6)$$

where C_{YbX} ($X = \text{Tm}$ or Yb) represents the energy-transfer microparameters. These microparameters are related to the energy-transfer probabilities P_{YbX} between two ions separated by a distance R by $P_{\text{YbX}}(R) = C_{\text{YbX}}/R^6$. The K_H parameter described by expression (6) is deduced by assuming a statistical distribution of acceptor and donor ions among the available sites in the host and a migration model with random hopping between the sensitizers. The hopping model seems well adapted when $C_{\text{YbYb}} > C_{\text{YbTm}}$. On the other hand, within the diffusion model developed by Yokota and Tanimoto, which applies when $C_{\text{YbYb}} < C_{\text{YbTm}}$, the energy-transfer probability remains linearly dependent versus $N_{\text{Tm}} \times N_{\text{Yb}}$ and $K_1 = K_D$ with

$$K_D = \{[16\pi^2/(3 \times 2^{3/4})] C_{\text{YbTm}}^{1/4} C_{\text{YbYb}}^{3/4}\} N_{\text{Tm}} N_{\text{Yb}}. \quad (7)$$

At this point, use can be made of the experimentally determined transfer probability K_1 . Thus, according to expression

TABLE IV. Microparameters $C_{\text{YbTm}}^{(1)}$ ($\text{cm}^6 \text{s}^{-1}$) for the energy-transfer step 1 in KY_3F_{10} and LiYF_4 .

	α_1	C_{YbYb}	$C_{\text{YbTm}}^{(1)}$ (Bürshtein)	$C_{\text{YbTm}}^{(1)}$ (Yokota)
KY_3F_{10}	1.87×10^{-38}	57.1×10^{-40}	1.54×10^{-40}	6.84×10^{-43}
LiYF_4	0.85×10^{-38}	36.3×10^{-40}	0.50×10^{-40}	1.14×10^{-43}

(4), the α_1 parameter could be used to derive values for the products of the microparameters appearing in expressions (6) and (7) and compare these products with those which can be obtained with the aid of the absorption and emission cross-section spectra of the transitions involved in the energy-transfer process, i.e.,

$$C_{\text{YbX}} = \frac{3c}{8\pi^4 n^2} \int \sigma_{\text{Ems}}^{\text{Yb}}(\lambda) \times \sigma_{\text{Abs}}^{\text{X}}(\lambda) d\lambda. \quad (8)$$

However, the overlap between the absorption and emission spectra of the Tm and Yb ions, respectively, is so weak that it is not possible to make this comparison as such. On the other hand, the absorption and emission cross-section spectra of the Yb ions, which enter into the calculation of the $\text{Yb} \leftrightarrow \text{Yb}$ migration parameter, overlap more strongly, as shown in Fig. 2, so that the C_{YbYb} value can be determined much more accurately. In the case of LiYF_4 , the absorption and emission spectra of Fig. 2 are averaged over the three polarizations while polarized spectra are given in Ref. 20. The microparameter was then found almost two times larger in KY_3F_{10} than in LiYF_4 ($C_{\text{YbYb}}(\text{KY}_3\text{F}_{10}) = 571 \times 10^{-41} \text{cm}^6 \text{s}^{-1}$ and $C_{\text{YbYb}}(\text{LiYF}_4) = 363 \times 10^{-41} \text{cm}^6 \text{s}^{-1}$). Consequently, use can be made in fact of the above expressions (6) and (7) to calculate and compare the $C_{\text{YbTm}}^{(1)}$ microparameters for the energy-transfer step 1 obtained with the two models, knowing the values of α_1 and C_{YbYb} from the fluorescence decay and spectral data, respectively. The results are presented in Table IV. The Burshtein model seems to lead to coherent results because the $C_{\text{YbTm}}^{(1)}$ parameter is smaller than the $\text{Yb} \leftrightarrow \text{Yb}$ migration parameter C_{YbYb} . On the other hand, the Yokota-Tanimoto model leads to a contradiction because in this case $C_{\text{YbTm}}^{(1)} \ll C_{\text{YbYb}}$ which is clearly not the domain of validity usually admitted for the diffusion model. The calculated decay curves using the microparameters of Table IV and the complete Burshtein model—also taking into account the direct energy transfer—are described by

$$I(t) = I_0 \exp\left(-\frac{t}{\tau} - \gamma\sqrt{t} - K_H t\right), \quad (9)$$

where $\gamma = \frac{4}{3} \pi^{3/2} C_{\text{YbTm}}^{1/2} N_{\text{Tm}}$. Because of the non-negligible effect of γ compared with K_H , this leads to nonexponential decays at short time, in contradiction with the experimental data (see Fig. 3). Therefore our conclusion is that the C_{YbTm} parameters calculated by using the Burshtein model are probably overestimated but remain interesting as indicative values for this type of nonresonant energy transfer. Moreover, it is clear, whatever the model considered, that the higher energy-transfer probability K_1 in KY_3F_{10} compared to LiYF_4 cannot be fully quantitatively attributed to the migra-

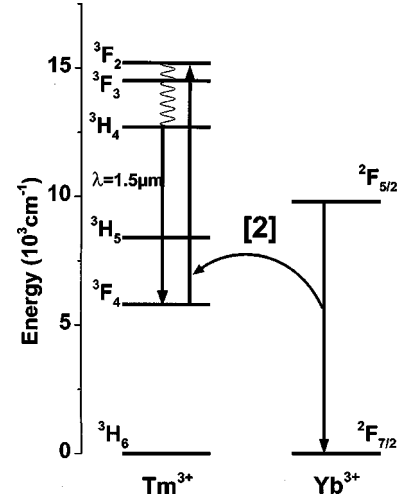


FIG. 5. Scheme for energy-transfer step 2 between Yb^{3+} and Tm^{3+} ions.

tion effects and that part of it must be attributed to the efficiency of the final Yb-Tm transfer step. Obviously, a critical criteria for multipolar interactions could be the average distance between the Yb and Tm ions. But, the distributions of the different sites surrounding a given position for a rare-earth ion are equivalent in both lattices. To find why C_{YbTm} could be higher in KY_3F_{10} , we have compared the energy mismatches between the emission spectra of the Yb^{3+} ions (transition ${}^2F_{5/2} \rightarrow {}^2F_{7/2}$) and the absorption spectra of the Tm^{3+} ions (transition ${}^3H_6 \rightarrow {}^3H_5$). For that, we have determined the Stark sublevel positions of the multiplets involved in the energy-transfer process and found $\Delta E = 1152 \text{cm}^{-1}$ in KY_3F_{10} and $\Delta E = 1311 \text{cm}^{-1}$ in LiYF_4 which effectively should favor the energy transfer in the case of KY_3F_{10} .

V. SECOND STEP ENERGY TRANSFER RESULTS

As shown in Fig. 5, in the second step—called step 2—energy transfer corresponds to the relaxation/excitation scheme

$${}^2F_{5/2}(\text{Yb}) + {}^3F_4(\text{Tm}) \rightarrow {}^2F_{7/2}(\text{Yb}) + {}^3F_{2,3}(\text{Tm}). \quad (10)$$

This energy transfer is then immediately followed by rapid multiphonon relaxations bringing the Tm^{3+} ions from the ${}^3F_{2,3}$ down to the 3H_4 level. The microparameter $C_{\text{YbTm}}^{(2)}$ for the second step energy transfer was directly estimated by recording the excited-state absorption (ESA) spectrum of Tm^{3+} in the appropriate spectral domain, i.e., in the spectral domain of the ${}^3F_4 \rightarrow {}^3F_{2,3}$ ESA transition around $1 \mu\text{m}$. The ESA measurements were performed after direct excitation into the 3F_4 level with a color center laser tuned at $\lambda = 1680 \text{nm}$ by using the pump probe technique described in Ref. 22. Figure 6 shows the resulting ESA spectra and the emission spectra of the Yb^{3+} ions (${}^2F_{5/2} \rightarrow {}^2F_{7/2}$). The overlap integrals then allow us to calculate the microparameters for the step 2: $C_{\text{YbTm}}^{(2)}(\text{KY}_3\text{F}_{10}) = 21.7 \times 10^{-41} \text{cm}^6 \text{s}^{-1}$ and $C_{\text{YbTm}}^{(2)}(\text{LiYF}_4) = 32.7 \times 10^{-41} \text{cm}^6 \text{s}^{-1}$. In this case, the direct energy transfer appears slightly more efficient in LiYF_4 than in KY_3F_{10} . However, the migration among the Yb^{3+} ions will appear as the dominant process and once again the overall energy transfer between the Yb^{3+} and Tm^{3+} ions will

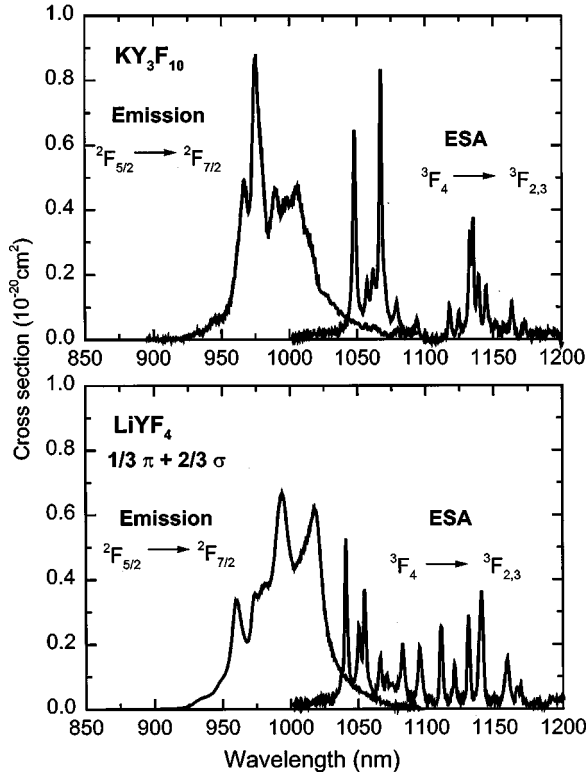


FIG. 6. Excited-state absorption spectrum of Tm^{3+} (${}^3F_4 \rightarrow {}^3F_{2,3}$) and emission spectrum of Yb^{3+} ions (${}^2F_{5/2} \rightarrow {}^2F_{7/2}$) in LiYF_4 and in KY_3F_{10} .

be enhanced in KY_3F_{10} . To fully characterize the step 2, the fluorescence decay curves from the ${}^2F_{5/2}$ level of the Yb^{3+} ions were recorded again after direct excitation with short laser pulses as a function of the excitation pulse energy. When the pump energy increases, the Tm^{3+} population in the 3F_4 level builds up and the second step gives a significant contribution to the fluorescence lifetime of the ${}^2F_{5/2}$ level which becomes progressively shorter. The fluorescence decay curves remain purely exponential which now enables us to deduce simply a value of the energy-transfer probability K_2 for the step 2 from the effective lifetime of ${}^2F_{5/2}$ level at low excitation density and at higher excitation density using

$$K_2(E) = \frac{1}{\tau({}^2F_{5/2})_E} - \frac{1}{\tau({}^2F_{5/2})_{E=0}}, \quad (11)$$

where E is the excitation density. Assuming that this second step energy transfer is mainly assisted by migration, one should obtain a linear dependence of the energy-transfer probability K_2 with the product $n({}^3F_4)_{\text{Tm}} \times N_{\text{Yb}}$, i.e.,

$$K_2 = \alpha_2 \times n({}^3F_4)_{\text{Tm}} \times N_{\text{Yb}}. \quad (12)$$

The evolution of K_2 versus the pumping density is reported in Fig. 7 for two samples of LiYF_4 . As can be seen in the figure, the energy-transfer probability is linearly dependent on the pumping density. This confirms the validity of relation (12) since if we assume in a first approximation a negligible depletion of the 3F_4 population because of energy-transfer step 2, the 3F_4 population density $n({}^3F_4)_{\text{Tm}}$ appears to be proportional to the pumping density. At higher pump

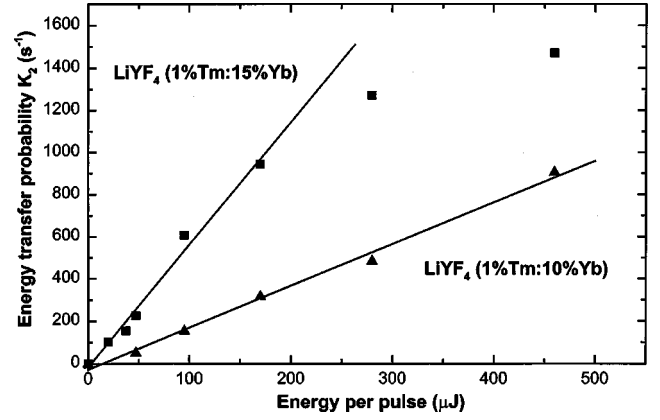


FIG. 7. Dependence of the energy-transfer probability K_2 of the energy-transfer step 2 on the excitation density at $\lambda = 960$ nm.

energy, K_2 is no longer proportional to the pumping density because the depletion of the 3F_4 level becomes preponderant.

To obtain a realistic value of α_2 , we have used two different methods to determine the energy-transfer parameter W_2 which is derived from formula (12):

$$W_2 = \alpha_2 \cdot N_{\text{Yb}}. \quad (13)$$

First, it is possible to modelize the observed lifetime shortening of the ${}^2F_{5/2}$ level by knowing the population density in the ${}^2F_{5/2}$ level with a good accuracy. We thus placed an aperture of $400 \mu\text{m}$ in front of the sample to impose the geometry of the excitation. Then, the incident energy was measured with a joulemeter positioned behind the aperture. Using the previously calculated energy-transfer parameter W_1 for the step 1 and knowing the exact excitation geometry, the reduction of the lifetime of the ${}^2F_{5/2}$ level was fitted with a classical rate equation model and the energy-transfer parameter W_2 was deduced. As we noticed above, the fluorescence decay curves of the ${}^2F_{5/2}$ level still remain exponential even at high pumping density. This is the main characteristic which justifies the use of the rate equation model to describe the Yb luminescence dynamics. This rate equation model is given by

$$\begin{aligned} \frac{dn({}^2F_{5/2})}{dt} = & -\frac{n({}^2F_{5/2})}{\tau({}^2F_{5/2})} - W_1 \cdot n({}^3H_6) \cdot n({}^2F_{5/2}) \\ & - W_2 \cdot n({}^3F_4) \cdot n({}^2F_{5/2}) + W_3 \cdot n({}^3H_4) \cdot n({}^2F_{7/2}) \\ & + \frac{P \cdot \sigma_{\text{abs}}}{h \cdot \nu \cdot S} \cdot n({}^2F_{7/2}), \end{aligned}$$

$$\begin{aligned} \frac{dn({}^3F_4)}{dt} = & -\frac{n({}^3F_4)}{\tau({}^3F_4)} + \frac{n({}^3H_4) \cdot \beta}{\tau({}^3H_4)} + W_1 \cdot n({}^3H_6) \cdot n({}^2F_{5/2}) \\ & - W_2 \cdot n({}^3F_4) \cdot n({}^2F_{5/2}) \\ & + 2 \cdot W_{\text{SQ}} \cdot n({}^3H_6) \cdot n({}^3H_4), \end{aligned}$$

$$\begin{aligned} \frac{dn({}^3H_4)}{dt} = & -\frac{n({}^3H_4)}{\tau({}^3H_4)} + W_2 \cdot n({}^3F_4) \cdot n({}^2F_{5/2}) \\ & - W_{\text{SQ}} \cdot n({}^3H_6) \cdot n({}^3H_4) - W_3 \cdot n({}^3H_4) \cdot n({}^2F_{7/2}) \end{aligned}$$

with

$$N_{\text{Yb}} = n(^2F_{7/2}) + n(^2F_{5/2}),$$

$$N_{\text{Tm}} = n(^3H_6) + n(^3H_4) + n(^3F_4), \quad (14)$$

where $\tau(^2F_{5/2})$, $\tau(^3F_4)$, and $\tau(^3H_4)$ are the lifetimes at low concentration of the $^2F_{5/2}$, 3F_4 and 3H_4 levels, β is the branching ratio of transitions which populate the 3F_4 level starting from the 3H_4 level ($^3H_4 \rightarrow ^3H_5$ and $^3H_4 \rightarrow ^3F_4$), P is the pump power, S is the area of the pump spot into the crystal, $h\nu$ is the energy of the pump photons, and σ_{abs} is the absorption cross section at the pump wavelength. The W_3 parameter refers to the back transfer from Tm^{3+} to Yb^{3+} ions [$^3H_4(\text{Tm}) + ^2F_{7/2}(\text{Yb}) \rightarrow ^3H_6(\text{Tm}) + ^2F_{5/2}(\text{Yb})$] and W_{SQ} is the energy-transfer parameter of the so-called ‘‘self-quenching’’ process [$^3H_4(\text{Tm}) + ^3H_6(\text{Tm}) \rightarrow ^3F_4(\text{Tm}) + ^3F_4(\text{Tm})$]. The W_3 and W_{SQ} parameters are determined independently as it will be explained in the next part of this paper.

To confirm this first approach, a second method was used. It consisted in recording the buildup kinetic of the fluorescence from $^2F_{5/2}$ after a long pulse excitation at $\lambda = 960$ nm. The current injected in an InGaAs laser diode was directly modulated by an external generator to create a square pulse with a negligible rise time compared to the relaxation times involved in the evolution of $n(^2F_{5/2})_{\text{Yb}}$ and a pulse duration long enough to reach an asymptotic value. The incident beam profile of the laser diode can be described by an asymmetric Gaussian distribution. This geometrical factor is important here since this second energy transfer is a nonlinear process. This implies that the main difficulty for step 2 is to determine exactly the $^2F_{5/2}$ excited-state spatial distribution. Figure 8 shows that an evolution of the buildup kinetics of the $^2F_{5/2}$ level population can be observed when the incident pumping density increases. Under limited excitation densities, the kinetics of the $^2F_{5/2}$ level tends to an asymptotic value only fixed by the linear de-excitation processes affecting $^2F_{5/2}$ (radiative transitions and step 1). Under intense square-pulse excitation, we can observe that the luminescence curve rapidly increases up to a maximum and then slowly decays to reach an asymptotic value significantly lower than the maximum. This is due to the greater efficiency of the up-conversion step 2 which depends on the pumping rate. This maximum appears to be more pronounced in KY_3F_{10} than in LiYF_4 which suggests that up-conversion energy-transfer step 2 is more efficient in KY_3F_{10} than in LiYF_4 . For each sample, a second assessment of W_2 was obtained by fitting the rate equation model to the Yb luminescence buildup at several pumping densities. As can be seen in Fig. 8, this modelization is in very good agreement with the experimental data, especially for the samples with Yb concentration around 5% in LiYF_4 and KY_3F_{10} increasing the incident pumping density from 5 to 700 W/cm^2 . For Yb concentrations above 10%, the simulation of the luminescence kinetics is not so satisfying throughout the range of pumping densities because shorter average distances between the Yb ions favor higher-order up-conversion processes starting from the 3H_4 level. In order to minimize the influence of such up-conversion energy transfers in the determination of the energy-transfer parameter W_2 , the simu-

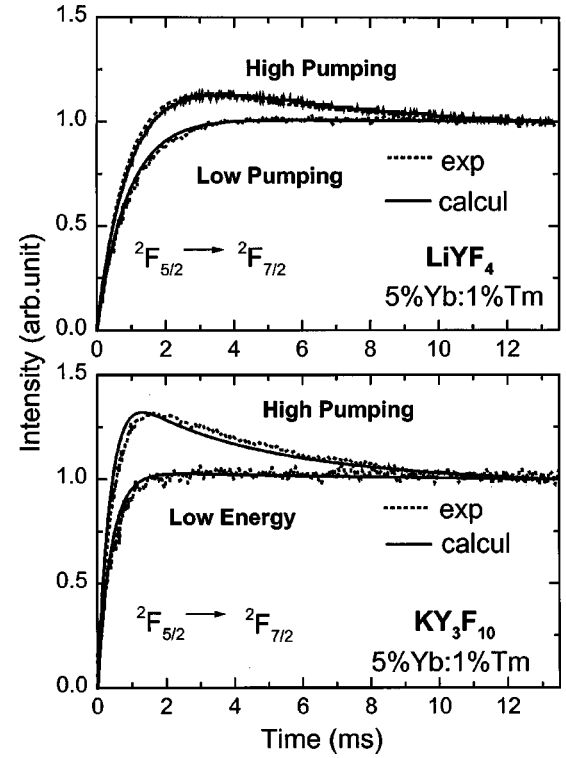


FIG. 8. Luminescence buildup kinetics of the $^2F_{5/2}$ level under weak and intense square-pulsed excitations of LiYF_4 and KY_3F_{10} .

lation was carried out only for weak to moderate excitation densities (below 70 W/cm^2). Values of W_2 derived by using both methods are listed in Table V for LiYF_4 and KY_3F_{10} . Systematic errors are associated with all parameters necessary to describe the exact excited-state profile involved in these experiments. However, the results of both methods reasonably agree which validate the treatment used to describe the step 2. W_2 turns out to be larger in KY_3F_{10} than in LiYF_4 which confirms the preponderance of the migration energy process in the second step. The value of W_2 obtained in BaY_2F_8 and also reported in Table V is smaller than in LiYF_4 . It suggests that the step 2 is not very efficient in this

TABLE V. Parameters W_2 ($10^{-18} \text{ cm}^{-3} \text{ s}^{-1}$) for energy-transfer step 2 obtained by using methods 1 and 2. Method 1 gives the W_2 values obtained by fitting the rate equations to the Yb decay curves and method 2 the values derived by fitting the rate equations to the Yb buildup luminescence kinetics.

Sample	W_2 (method 1)	W_2 (method 2)
LiYF_4 :0.5% Tm:5% Yb (no. 2)	110	40
LiYF_4 :0.5% Tm:7% Yb (no. 3)	185	90
LiYF_4 :1% Tm:5% Yb (no. 4)	140	120
LiYF_4 :1% Tm:10% Yb (no. 5)	300	400
LiYF_4 :1% Tm:15% Yb (no. 6)	600	450
KY_3F_{10} :0.5% Tm:5% Yb (no. 8)	250	340
KY_3F_{10} :1% Tm:5% Yb (no. 9)	260	470
BaY_2F_8 :0.5% Tm:5% Yb (no. 11)	35	

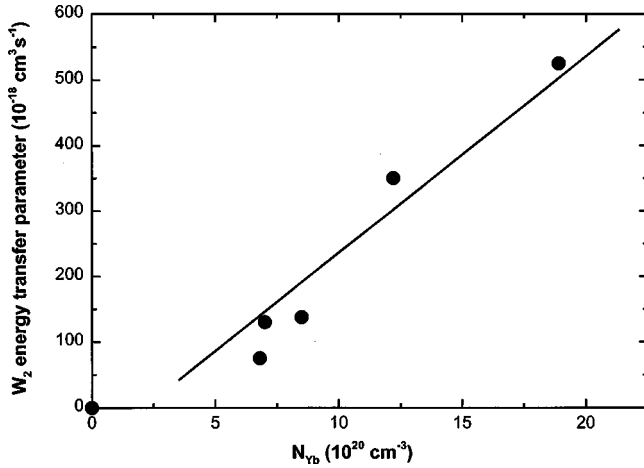


FIG. 9. Dependence of the parameter W_2 of the energy-transfer step 2 on the Yb^{3+} ion concentration in LiYF_4 .

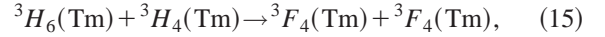
crystal. Average values for the energy-transfer parameter W_2 were then derived from the results of methods 1 and 2 for each sample. Figure 9 shows the evolution of this average energy-transfer parameter W_2 versus Yb concentration in LiYF_4 . As can be seen, the linear dependence of W_2 versus Yb concentration predicted by Eq. (13) is in quite good agreement with the observed results. The calculation of the slope yields $\alpha_2 = 30 \times 10^{-38} \text{ cm}^6 \text{ s}^{-1}$. In Fig. 9, the linear regression leads to an initial value of $N_{\text{Yb}} = 2.1 \times 10^{20} \text{ cm}^{-3}$ which has no physical meaning since the theoretical value for $W_2 = 0$ should be, of course, $N_{\text{Yb}} = 0$. This discrepancy might arise from the model of migration assisted up-conversion energy transfer: at low Yb concentration, a large distance between two neighboring Yb ions would lead to a limitation of migration energy processes which implies that below a critical Yb concentration, up-conversion energy-transfer step 2 cannot be described any longer in terms of $W_2 \times n(^3F_4)_{\text{Tm}} \times n(^2F_{5/2})_{\text{Yb}}$ as usually used in the rate equation model, as it has been recently explained by Zubenko and Noginov.²⁶

Another way to estimate α_2 is simply to apply the Burshstein model—expression (6)—using the $C_{\text{YbTm}}^{(2)}$ derived from the overlap integral. The calculation leads to a value of $\alpha_2 = 2.2 \times 10^{-38} \text{ cm}^6 \text{ s}^{-1}$ which is much smaller than the value of $30 \times 10^{-38} \text{ cm}^6 \text{ s}^{-1}$ experimentally obtained. A part of the explanation could be that the part of phonon-assisted energy transfer is not negligible in step 2. Therefore the value of $C_{\text{YbTm}}^{(2)}$ is certainly underestimated since these phonon-assisted energy transfers do not appear into the calculation of the spectral overlap integral [formula (8)]. However, this explanation is not sufficient to account for the discrepancy between the value of α_2 calculated by using the Burshtein model and the value derived from the methods 1 and 2. So, the Burshtein model appears not well adapted to predict the energy-transfer probability K_2 . But, this model remains useful to give orders of magnitude.

VI. SELF-QUENCHING AND THIRD STEP ENERGY-TRANSFER RESULTS

To obtain a full description of the fluorescence dynamics in the (Yb, Tm) codoped systems, it is necessary to take into

account the cross relaxation which occurs among the Tm ions, i.e.,



usually called self-quenching. This process leads to a reduction of the lifetime of 3H_4 which limits the energy storage into the emitting 3H_4 level for the 1.5- or the 2.3- μm laser transition. Decay curves of the 3H_4 level at very low Tm concentration and at $N_{\text{Tm}} = 1\%$ in singly doped and codoped samples were registered and compared. A nonexponential decay is observed at the beginning of the decay curve for $N_{\text{Tm}} = 1\%$ which clearly indicates that direct energy transfers between nearest-neighboring ions occur. Because of this nonexponential character, the effective 3H_4 lifetime was obtained by normalizing to unity the fluorescence decay curves at time $t=0$, by integrating over the entire decay curves and by using the expression

$$\tau_f = \frac{1}{I_0} \int_0^\infty I(t) dt \quad (16)$$

in which I_0 is the fluorescence intensity at $t=0$. By this way, the measured 3H_4 lifetime was found equal to 1.2 ms at $N_{\text{Tm}} = 1.2 \times 10^{20} \text{ cm}^{-3}$ in LiYF_4 , 0.95 ms at $N_{\text{Tm}} = 1.37 \times 10^{20} \text{ cm}^{-3}$ in KY_3F_{10} and 1.32 ms at $N_{\text{Tm}} = 1.08 \times 10^{20} \text{ cm}^{-3}$ in BaY_2F_8 . Combining these results with the 3H_4 lifetime at very low concentration (2, 1.9, and 2.2 ms in LiYF_4 , KY_3F_{10} , and BaY_2F_8 , respectively), we deduced the self-quenching probability K_{SQ} . The self-quenching process between the Tm ions was previously investigated²⁷ and a quadratic dependence of the self-quenching probability K_{SQ} on the dopant concentration was observed:

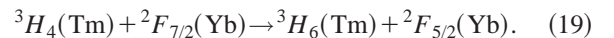
$$K_{\text{SQ}} = \alpha_{\text{SQ}} \times N_{\text{Tm}}^2 \quad (17)$$

and therefore

$$W_{\text{SQ}} = \alpha_{\text{SQ}} \times N_{\text{Tm}}. \quad (18)$$

Relation (17) then leads to $\alpha_{\text{SQ}} = 2.3 \times 10^{-38} \text{ cm}^6 \text{ s}^{-1}$ in LiYF_4 and $\alpha_{\text{SQ}} = 2.8 \times 10^{-38} \text{ cm}^6 \text{ s}^{-1}$ in KY_3F_{10} . The self-quenching seems to be slightly stronger in KY_3F_{10} than in LiYF_4 . This result is consistent with the Stark sublevel positions of the multiplets involved in the self-quenching since the energy mismatch in LiYF_4 is larger ($\Delta E = 655 \text{ cm}^{-1}$) than in KY_3F_{10} ($\Delta E = 505 \text{ cm}^{-1}$). In BaY_2F_8 , α_{SQ} is of the order of $1.43 \times 10^{-38} \text{ cm}^6 \text{ s}^{-1}$. It shows that the efficiency of the self-quenching is quite weak in BaY_2F_8 .

The 3H_4 level population is also affected by another energy transfer—denoted step 3—which corresponds to



This third step back transfer described in Fig. 10 is obviously a detrimental energy transfer which reduces the lifetime of the emitting 3H_4 level. Following the same method used to quantify step 1, it is possible to calculate the energy-transfer probability K_3 by using the expression

$$K_3 = \frac{1}{\tau({}^3H_4)_{\text{Yb-Tm}}} - \frac{1}{\tau({}^3H_4)_{\text{Tm}}}, \quad (20)$$

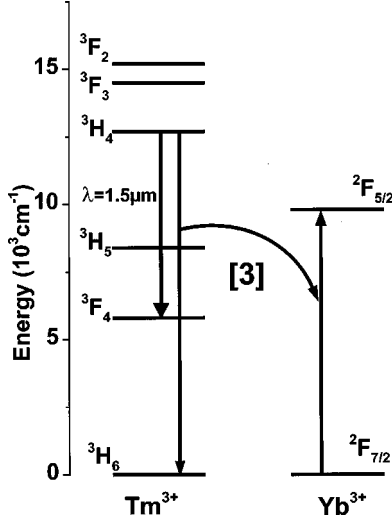


FIG. 10. Scheme for energy-transfer step 3 between Yb^{3+} and Tm^{3+} ions.

where $\tau(^3H_4)_{\text{Tm}}$ and $\tau(^3H_4)_{\text{Tm-Yb}}$ correspond to the effective lifetimes for the singly doped and codoped samples, respectively. The energy mismatch involved in this transfer is very large: $\Delta E = 2650 \text{ cm}^{-1}$ in KY_3F_{10} and $\Delta E = 2520 \text{ cm}^{-1}$ in LiYF_4 . However, the back transfer is enhanced by the high Yb concentration which provides a very short average Yb-Tm distance. For example, with the sample $\text{LiYF}_4(\text{Tm}1\%:\text{Yb}15\%)$, the calculation of the energy-transfer efficiency for step 3 using

$$\eta_3 = \frac{K_3}{K_1 + 1/\tau(^3H_4)_{\text{Tm}}} \quad (21)$$

yields $\eta_3 = 60\%$. The back-transfer probability K_3 is plotted as a function of the product $N_{\text{Tm}} \times N_{\text{Yb}}$ in Fig. 11 for LiYF_4 and KY_3F_{10} . A linear dependence of K_3 versus $N_{\text{Tm}} \times N_{\text{Yb}}$ is observed which indicates that the back transfer can be assigned to be a migration-controlled energy transfer even if the presence of direct energy transfers is attested by the non-exponential character of the 3H_4 decay curve. From the slope presented in Fig. 11, we deduced a value of α_3 equal to

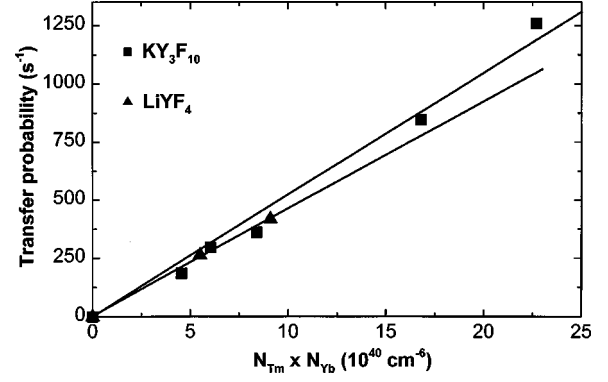


FIG. 11. Variation of the energy-transfer probability K_3 of the energy-transfer step 3 as a function of the product $N_{\text{Tm}} \times N_{\text{Yb}}$.

$0.58 \times 10^{-38} \text{ cm}^6 \text{ s}^{-1}$ in LiYF_4 and $0.46 \times 10^{-38} \text{ cm}^6 \text{ s}^{-1}$ in KY_3F_{10} . Step 3 appears to be slightly more efficient in LiYF_4 than in KY_3F_{10} . This confirms the values of energy mismatch mentioned above where ΔE is smaller in LiYF_4 than in KY_3F_{10} . Moreover, the energy-transfer parameter W_3 , introduced in the rate equation model, can be connected to α_3 by the expression

$$W_3 = \alpha_3 \cdot N_{\text{Tm}}. \quad (22)$$

Table VI lists all the calculated values of W_3 . The results show that the back transfer is about of the same order of magnitude in LiYF_4 and in BaY_2F_8 .

Finally, the energy-transfer parameters W_i ($i=1-3$ and $i=\text{SQ}$) could be calculated using α_i for different concentrations of Tm and Yb. It implies however, as shown above, that the Yb concentration is kept in a limited domain corresponding to the migration assisted regime ($N_{\text{Yb}} \geq 3\%$) but still below the fast migration regime ($N_{\text{Yb}} \leq 10\%$).

VII. LASER THRESHOLD SIMULATION AND LASER EXPERIMENTS

For an end-pumped solid-state laser, the threshold corresponds to a round-trip gain averaged over the cavity mode—

TABLE VI. Lifetimes of the 3H_4 level in singly doped crystals and codoped with Yb^{3+} and Tm^{3+} and energy-transfer parameters W_3 ($10^{-18} \text{ cm}^{-3} \text{ s}^{-1}$) for energy-transfer step 3.

Sample	$\tau(^3H_4)_{\text{Tm}}$ (msec)	$\tau(^3H_4)_{\text{Tm-Yb}}$ (msec)	W_3
$\text{LiYF}_4:1\% \text{ Tm}$ (no. 1)	1.2		
$\text{LiYF}_4:0.5\% \text{ Tm}:5\% \text{ Yb}$ (no. 2)	1.66	1.27	0.27
$\text{LiYF}_4:0.5\% \text{ Tm}:7\% \text{ Yb}$ (no. 3)	1.63	1.1	0.35
$\text{LiYF}_4:1\% \text{ Tm}:5\% \text{ Yb}$ (no. 4)	1.2	0.84	0.51
$\text{LiYF}_4:1\% \text{ Tm}:10\% \text{ Yb}$ (no. 5)	1.06	0.56	0.69
$\text{LiYF}_4:1\% \text{ Tm}:15\% \text{ Yb}$ (no. 6)	1.2	0.48	0.66
$\text{KY}_3\text{F}_{10}:1\% \text{ Tm}$ (no. 7)	0.95		
$\text{KY}_3\text{F}_{10}:0.5\% \text{ Tm}:5\% \text{ Yb}$ (no. 8)	1.47	1.06	0.35
$\text{KY}_3\text{F}_{10}:1\% \text{ Tm}:5\% \text{ Yb}$ (no. 9)	0.95	0.68	0.60
$\text{BaY}_2\text{F}_8:1\% \text{ Tm}$ (no. 10)	1.32		
$\text{BaY}_2\text{F}_8:0.5\% \text{ Tm}:5\% \text{ Yb}$ (no. 11)	1.58	1.25	0.24

TABLE VII. Parameters used in the laser experiment with Tm:Yb:LiYF₄ (1–10%) (sample 5).

Absorption coefficient: $\alpha = 7.4 \text{ cm}^{-1}$
Sample length: $L = 0.23 \text{ cm}$
Pump beam waist: $\omega_p = 46 \text{ }\mu\text{m}$
Laser beam waist: $\omega_1 = 30 \text{ }\mu\text{m}$
Energy-transfer parameters
$W_1 = 9.1 \times 10^{-18} \text{ cm}^3 \text{ s}^{-1}$, $W_2 = 350 \times 10^{-18} \text{ cm}^3 \text{ s}^{-1}$
$W_3 = 0.69 \times 10^{-18} \text{ cm}^3 \text{ s}^{-1}$; $W_{SQ} = 3.2 \times 10^{-18} \text{ cm}^3 \text{ s}^{-1}$

equal to the round-trip losses. This condition, given by Fan and Byer,²⁸ is expressed as

$$\delta = \int \int \int 2\sigma_{SE} L s_0(r, z) [n_2(r, z) - n_1(r, z) f_1 / f_2] dV, \quad (23)$$

where δ are the total losses per round trip, L the gain medium length, σ_{SE} the effective emission cross section, $n_2(r, z)$ and $n_1(r, z)$ are the population densities in the upper and the lower laser levels, f_2 and f_1 represent the fractional populations in the upper and lower Stark sublevels, and $s_0(r, z)$ is the normalized cavity mode assuming a TEM_{0,0} mode. We applied formula (23) for the ${}^3H_4 \rightarrow {}^3F_4$ laser transition in LiYF₄ in the CW regime. At $1.5 \text{ }\mu\text{m}$, the calculation of f_1 / f_2 yields a value of 0.38 (Ref. 13) and the effective emission cross section σ_{SE} is equal to $4 \times 10^{-21} \text{ cm}^2$. The spatial distributions of the population densities in the 3H_4 and 3F_4 levels are estimated by solving the rate equations given by formula (14) in the steady-state regime using the energy-transfer parameters defined above.

To check the validity of this treatment, we performed measurements of laser oscillation under the conditions listed in Table VII with a LiYF₄(Tm1%:Yb10%) sample. A laser threshold equal to 125 mW incident pump power in the crystal was obtained with an output mirror transmission of 2%. The result of this laser experiment is plotted in Fig. 12. The calculation of the round-trip gain averaged over the cavity mode for an incident pump power of 125 mW leads to a value of $\delta = 3.0\%$ using expression (23) and the rate equation model. This result implies detrimental losses per round trip of 1% which appears to be a realistic value. It is to be

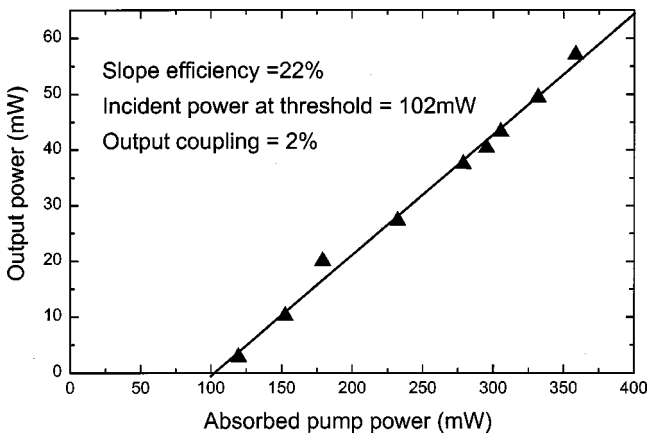


FIG. 12. Laser curve with a LiYF₄ (1% Tm:10% Yb) sample (experimental conditions are listed in Table VII).

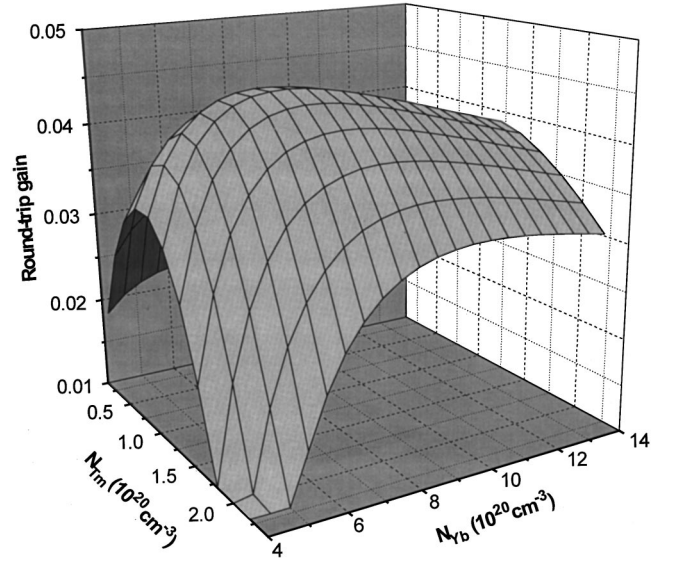


FIG. 13. Calculated dependence of the round-trip gain versus Yb and Tm concentrations at $\lambda = 1.5 \text{ }\mu\text{m}$ in LiYF₄.

noted that this value is overestimated since in this treatment we do not describe the losses due to the high-order up-conversion processes that become non-negligible and deplete the emitting 3H_4 level under laser experimental conditions. However, these losses are limited since, when the laser oscillation takes place at $1.5 \text{ }\mu\text{m}$, a significant reduction of the up-conversion luminescence intensity in the blue is observed, which corresponds to a diminution of the population in the 3H_4 level due to the stimulated emission at $1.5 \text{ }\mu\text{m}$.

Finally, expression (23) was used to optimize the Tm and Yb concentrations for the laser transition at $1.5 \text{ }\mu\text{m}$. Indeed, Eqs. (5), (13), (18), and (22) connected with expression (23) enable us to determine the round-trip gain as a function of the Yb and Tm concentrations. The laser threshold was estimated for the same incident pump power and therefore the crystal length was adjusted versus the Yb concentration so that 86% of the pump is absorbed by the sample. The round-trip gain averaged over the cavity mode is plotted in a three-dimensional graphic as a function of Yb and Tm concentrations in Fig. 13. It is important to note that the variation of Yb concentration was kept within the domain of validity of the Eqs. (5) and (13) mentioned above. As can be seen in Fig. 13, we found a gain maximum for $N_{Yb} = 8 \times 10^{20} \text{ cm}^{-3}$ and $N_{Tm} = 1.5 \times 10^{20} \text{ cm}^{-3}$. These optimized codopant concentrations show clearly that two types of energy transfers compete for the $1.5\text{-}\mu\text{m}$ laser transition: first, steps 1 and 2 which tend to populate the emitting 3H_4 level and second, step 3 and self-quenching which can be considered as detrimental for the laser emission. It can be also pointed out that the optimized value for the Yb concentration does not appear to be a critical parameter above 6% ($\approx 8.4 \times 10^{20} \text{ ions/cm}^3$). On the other hand, because of the self-quenching which strongly affects the 3H_4 lifetime, the Tm concentration must be kept around 1% ($\approx 1.4 \times 10^{20} \text{ ions/cm}^3$) to give the best laser performance.

Our modelization of the pump threshold can be used also to describe the laser emission at $2.3 \text{ }\mu\text{m}$ (transition ${}^3H_4 \rightarrow {}^3H_5$). Compared to the emission at $1.5 \text{ }\mu\text{m}$ (transition ${}^3H_4 \rightarrow {}^3F_4$), the only differences in expression (23) are the

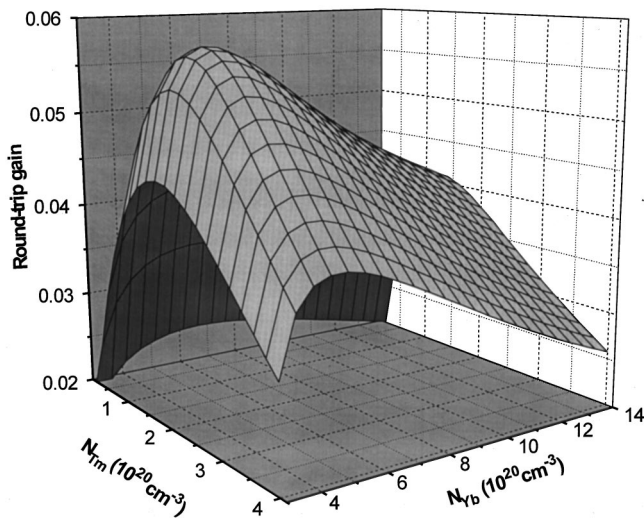


FIG. 14. Calculated dependence of the round-trip gain versus Yb and Tm concentrations at $\lambda = 2.3 \mu\text{m}$ in LiYF_4 .

stimulated emission cross section ($\sigma_{\text{SE}} = 5.6 \times 10^{-21} \text{ cm}^2$) and the fact that $n_1(r, z)$ is now equal to zero because of the very fast deexcitation of the 3H_5 terminal level via multiphonon relaxation. The round-trip gain at $2.3 \mu\text{m}$ is plotted in Fig. 14 as a function of Yb and Tm concentrations. The optimized concentrations for this laser transition turn out to be $N_{\text{Yb}} = 5 \times 10^{20} \text{ cm}^{-3}$ and $N_{\text{Tm}} = 2 \times 10^{20} \text{ cm}^{-3}$. The absence of bottlenecking effect at $2.3 \mu\text{m}$ explains why the optimized Yb concentration is smaller than in the case of the $1.5\text{-}\mu\text{m}$ laser operation. Therefore the dependence on Yb concentration appears to be critical above $N_{\text{Yb}} = 5 \times 10^{20} \text{ cm}^{-3}$ since an increase of Yb concentration leads to an increase of the back-transfer effect which reduces the gain of the laser transition. On the other hand, the optimized Tm concentration is slightly larger than in the case of the $1.5\text{-}\mu\text{m}$ transition. This can be explained by the fact that the self-quenching reinforces the bottlenecking effect at $1.5 \mu\text{m}$ by filling the terminal level 3F_4 which is not the case at $2.3 \mu\text{m}$.

Moreover, considering the same incident pump power for both laser transitions, the round-trip gain is always larger at $2.3 \mu\text{m}$ than at $1.5 \mu\text{m}$ because of two main reasons: the larger emission cross section and the four-level character of the $2.3\text{-}\mu\text{m}$ laser transition.

VIII. CONCLUSION

We have performed a spectroscopic and dynamic study of various (Yb, Tm) codoped systems. The purpose was to give values for the three main energy-transfer parameters necessary to describe the 1.5- and $2.3\text{-}\mu\text{m}$ laser transitions in three different crystals of KY_3F_{10} , LiYF_4 , and BaY_2F_8 . In addition to these three main energy transfers, we also have accounted for the self-quenching process which occurs between the Tm^{3+} ions and depletes the 3H_4 laser emitting level. The results show notable differences between the three studied crystals: the energy-transfer steps 1 and 2 which bring the excitation of the Tm^{3+} ions into the 3H_4 level are much stronger in KY_3F_{10} than in LiYF_4 or in BaY_2F_8 , while the back-transfer and the self-quenching probabilities are about the same order of magnitude in the three crystals. The predominance of energy migration process in the (Yb, Tm) codoped systems is demonstrated which validates the use of a simple rate equation model. Moreover, the comparison with the classical migration assisted energy-transfer models confirms the experimentally observed dependence of the energy-transfer parameters on the Tm and Yb concentrations. Using the parameters determined through the analysis of the spectroscopic results in LiYF_4 , we also have performed a simulation of the round-trip laser gain at 1.5 and $2.3 \mu\text{m}$ as a function of the Tm and Yb concentrations. The optimum concentrations for both laser transitions turned out to be slightly different and appear to be particularly critical in the case of the $2.3\text{-}\mu\text{m}$ laser, while the Yb concentration can be chosen in a larger range of values for the $1.5\text{-}\mu\text{m}$ laser transition. Further laser experiments are now underway including the use of crystals with these optimal codopant concentrations and the investigation of other materials such as LiLuF_4 .

- ¹F. Auzel, C. R. Académie des Sciences Paris **262**, 1016 (1966).
- ²L. Esterowitz, J. Noonan, and J. Bahler, Appl. Phys. Lett. **10**, 126 (1967).
- ³R. A. Heaves and J. F. Sarver, Phys. Rev. **182**, 427 (1969).
- ⁴S. A. Pollack, D. B. Chang, I. Fu Shih, and R. Tseng, Appl. Opt. **26**, 4400 (1987).
- ⁵E. Downing, L. Hesselink, J. Ralston, and R. MacFarlane, Science **273**, 1185 (1996).
- ⁶L. F. Johnson and H. J. Guggenheim, Appl. Phys. Lett. **19**, 44 (1971).
- ⁷R. A. MacFarlane, J. Phys. IV **4**, C4-289 (1994), and references therein.
- ⁸H. Sheife, T. Sandrock, E. Heumann, and G. Huber, OSA Trends in Optics and Photonics, edited by C. Pollock and W. R. Bosenberg (OSA, Washington, DC, 1997), Vol. 10.
- ⁹F. Heine, V. Ostroumov, E. Heumann, T. Jensen, G. Huber, and B. H. T. Chai, OSA Proc. Adv. Solid-State Lasers **24**, 77 (1995).
- ¹⁰A. Diening, P. E.-A. Möbert, and G. Huber, J. Appl. Phys. **84**, 5900 (1998).
- ¹¹X. X. Zhang, P. Hong, M. Bas, and B. H. T. Chai, Phys. Rev. B **51**, 9298 (1995).
- ¹²M. A. Noginov, M. Curley, P. Venkateswarlu, A. Williams, and H. P. Jentsen, J. Opt. Soc. Am. B **14**, 2126 (1997).
- ¹³A. Braud, S. Girard, J. L. Doualan, and R. Moncorgé, IEEE J. Quantum Electron. **34**, 2246 (1998).
- ¹⁴R. Yu. Abdulsabirov, M. A. Dubinskii, B. N. Kazakov, N. I. Silkin, and Sh. I. Yagudin, Kristallografiya **32**, 951 (1987) [Sov. Phys. Crystallogr. **32**, 559 (1987)].
- ¹⁵B. Chai, J. Lefaucheur, A. Pham, G. Lutts, and J. Nicholls, Proc. SPIE **1863**, 131 (1993).
- ¹⁶P. Rogin and J. Hullinger, J. Cryst. Growth **179**, 551 (1997).
- ¹⁷B. P. Sobolev and N. L. Tkachenko, J. Less-Common Met. **85**, 155 (1982).
- ¹⁸R. J. Trash and L. F. Johnson, J. Opt. Soc. Am. B **11**, 881 (1994).
- ¹⁹R. A. MacFarlane, J. Opt. Soc. Am. B **11**, 871 (1994).
- ²⁰L. D. DeLoach, S. A. Payne, L. L. Chase, L. K. Smith, W. L. Kway, and W. F. Krupke, IEEE J. Quantum Electron. **29**, 1179 (1993).

- ²¹D. S. Sumida and T. Y. Fan, *Opt. Lett.* **19**, 1343 (1994).
- ²²J. L. Doualan, P. Leboulanger, S. Girard, J. Margerie, F.-S. Erneux, and R. Moncorgé, *J. Lumin.* **72–74**, 179 (1997).
- ²³M. Yokota and O. Tanimoto, *J. Phys. Soc. Jpn.* **22**, 779 (1967).
- ²⁴A. I. Burshtein, *Zh. Eksp. Teor. Phys.* **62**, 1695 (1972) [*Sov. Phys. JETP* **35**, 882 (1972)].
- ²⁵S. A. Payne, L. L. Chase, L. K. Smith, W. L. Kway, and W. F. Krupke, *IEEE J. Quantum Electron.* **28**, 2619 (1992).
- ²⁶D. A. Zubenko and M. A. Noginov, *Phys. Rev. B* **55**, 8881 (1997).
- ²⁷G. Armagan, A. M. Buoncristiani, and B. Di Bartolo, *Opt. Mater.* **1**, 11 (1992).
- ²⁸T. Y. Fan and R. L. Byer, *IEEE J. Quantum Electron.* **23**, 605 (1987).